# SUPPLEMENTARY FIGURES

**Table S1.** RIEs determined during several calibrations at MRS-LCP supersite.

| *Calibrations* | $RIE_{NH4}$ | $RIE_{SO4}$ |
|---|---|---|
| *05/19/2017* | 3.3 | 0.92-0.98 |
| *06/28/2018* | 2.4 | 0.8-0.9 |
| *07/12/2018* | 3 | 0.91 |

**Table S2.** Detection limit in µg/m$^3$ (3*σ) of chemical species from ToF-ACSM:

| Ammonium | Nitrate | Organic | Sulfate | Chlore |
|---|---|---|---|---|
| 0.098 | 0.018 | 0.55 | 0.034 | 0.021 |

**Equation S1.** Pieber correction: True_CO2+(t) = measured_CO2+(t) **-** b*NO(t)+ **-** b*NO2+(t)

**Table S3.** Overview of b value used for Pieber correction and NO2+/NO+ ratio measured during ToF-ACSM calibrations:

| **Calibrations (mm/yy)** | **b (Pieber effect)** | **NO2+/NO+** |
|---|---|---|
| 12/16 | 0.0053 | 0.5631 |
| 05/17 | 0.0039 | 0.5604 |
| 06/18 | 0.0011 | 0.5730 |
| 12/18 | 0.0022 | 0.5604 |
| Average | **0.0032** | **0.5642** |
| Standard errors | **0.0009** | **0.0244** |

**Equation S2.** $NO^+$ = 30,-frag_air[30], frag_organic[30],-0.215*frag_organic[29]

$NO_2^+$ = 46,-0.127*45

| Spring | | Summer | | Autumn | | Winter | |
|---|---|---|---|---|---|---|---|
| lower | upper | lower | upper | lower | upper | lower | upper |
| 0.18 | 0.28 | 0.06 | 0.10 | 0.11 | 0.17 | 0.14 | 0.2 |

**Table S4.** Overview of ON/OA ratio (nitrated organics vs organic aerosol) for all seasons. Lower and upper bounds correspond to an assumed molecular weight for particle-phase organic nitrate of 200 and 300 g $mol^{-1}$, respectively.

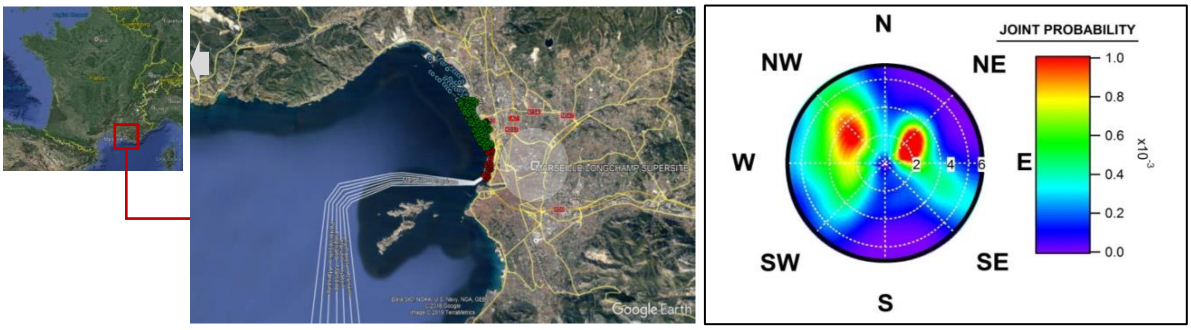


**Figure S1.** The map on the left shows the location of the supersite MRS-LCP (white square). The grey arrow indicates the industrial area location and coloured dots correspond to ship positions from different basins in Marseille port: red dots are for south basin, green for east basin, and blue for north basin. On the right the joint probability of wind speed and wind direction is represented for the full study period. Map provided by Google Earth Pro v7.3.3.7786, Data SIO, NOAA, U.S. Navy., NGA, GEBCO © 2020 Google.

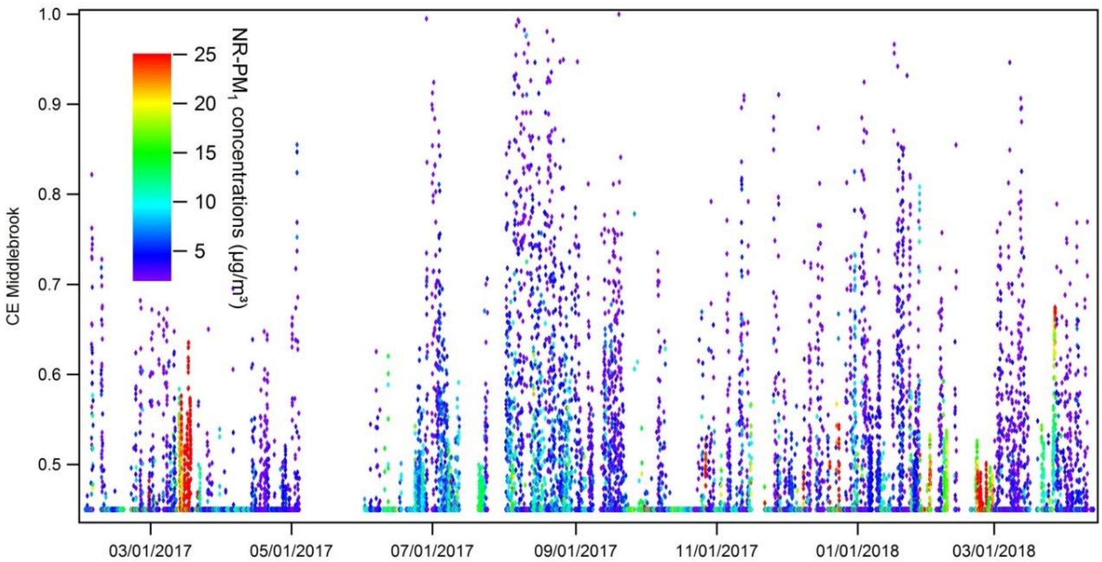


**Figure S2.** Time serie of collection efficiency (CE) from Middlebrook calculations coloured according to the NR-PM1 concentrations, for the full period of ACSM measurements.

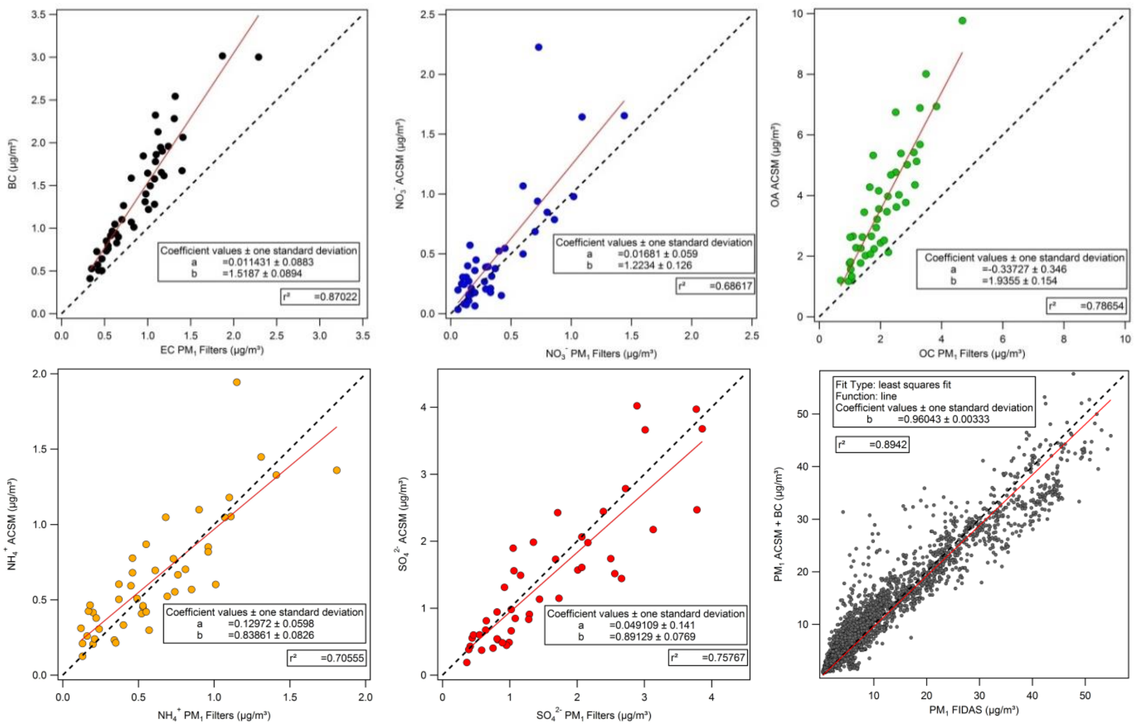


**Figure S3.** BC and ACSM species concentrations vs $PM_1$ 24h filters analysed respectively for EC, nitrate, OC (compared to organic matter from ACSM measurements), ammonium and sulfate. Reconstructed PM1 (ACSM+BC) are also compared to PM1 measurements from the FIDAS for a 3 months from February to April 2018. Red lines correspond to least squares fits between species and filters.

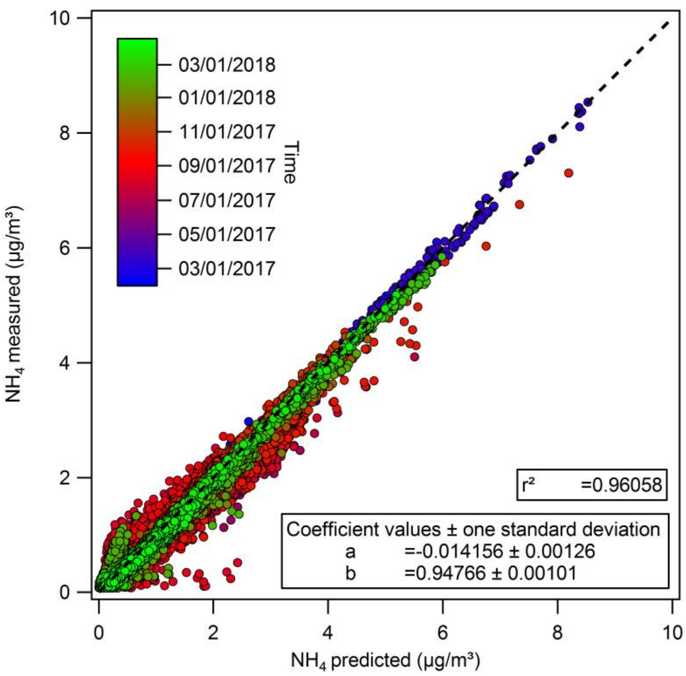


**Figure S4.** $NH_4$ measured (directly from TOF-ACSM) vs $NH_4$ predicted (calculated from $Cl^-$, $NO_3^-$ and $SO_4^{2-}$) for ionic balance evaluation. Black dashed-line is the 1:1 line and the fit coefficients are from least squares fit.

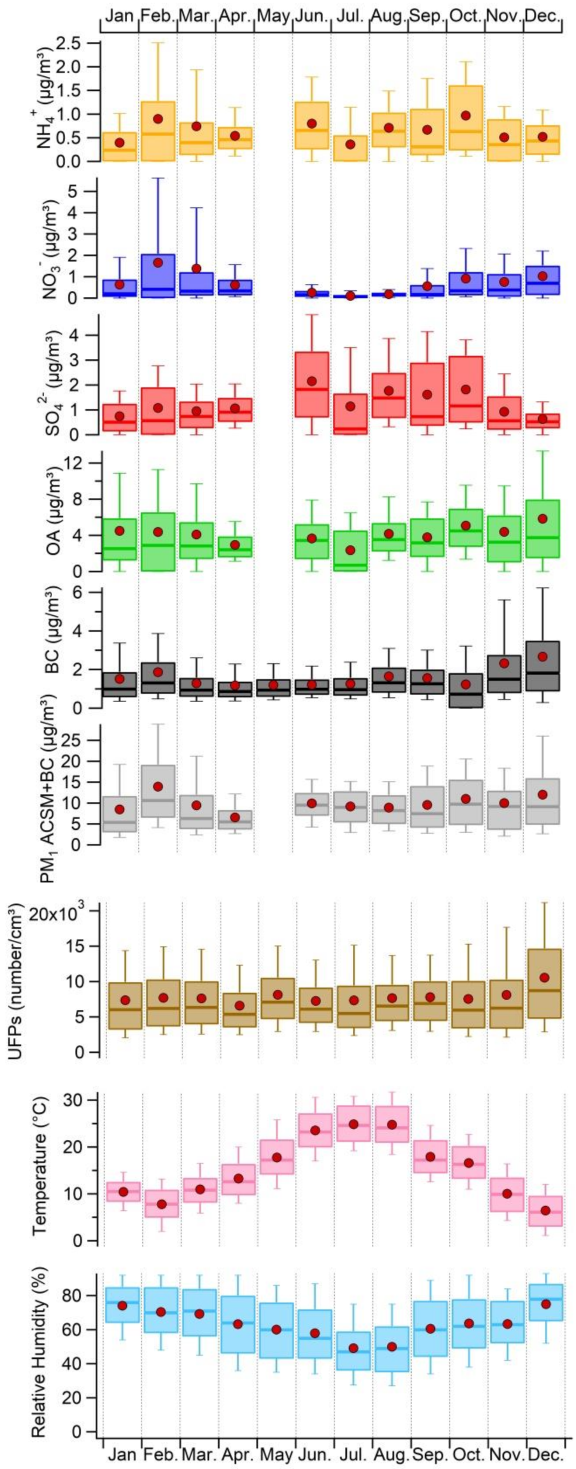


**Figure S5.** Monthly box plots of $PM_1$ chemical species, total $PM_1$ concentrations, UFPs (20-100nm) from 3031 monitor, temperature and relative humidity (from the Vaudran station). The band inside the box is the median (50$^{th}$ percentile), the bottom and top of the box represent the lower and upper quartiles respectively (the 25$^{th}$ and the 75$^{th}$ percentile). The ends of the whiskers denote here the 10$^{th}$ and 90$^{th}$ percentile. The red dots refer to the mean of each component.

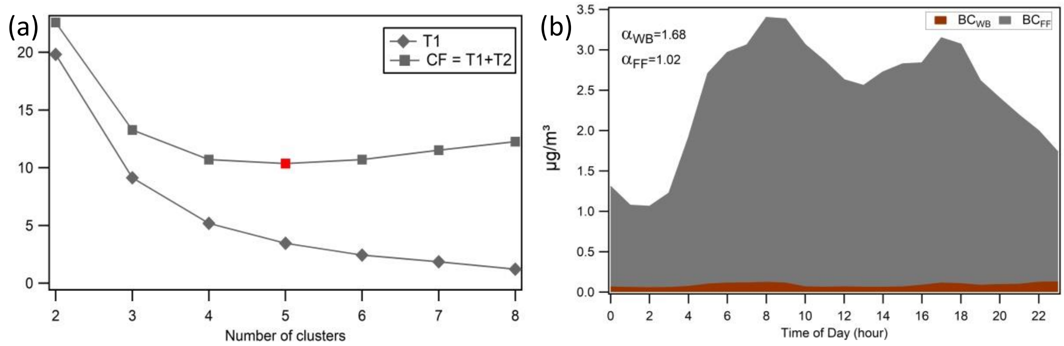


**Figure S6.** (a) Number of cluster selection according to T1 (diamond markers) and the cost function (T1+T2) (square markers). The red marker represents the minimum value and thus the number of cluster selected. (b) Diurnal evolutions of $BC_{WB}$ and $BC_{FF}$ recorded at kerbside "Kaddouz" site during summer 2017. Sensitivity analyses were performed on $\alpha_{WB}$ and $\alpha_{FF}$ combinations in the aethalometer model to evaluate most realistic patterns for the two sources.

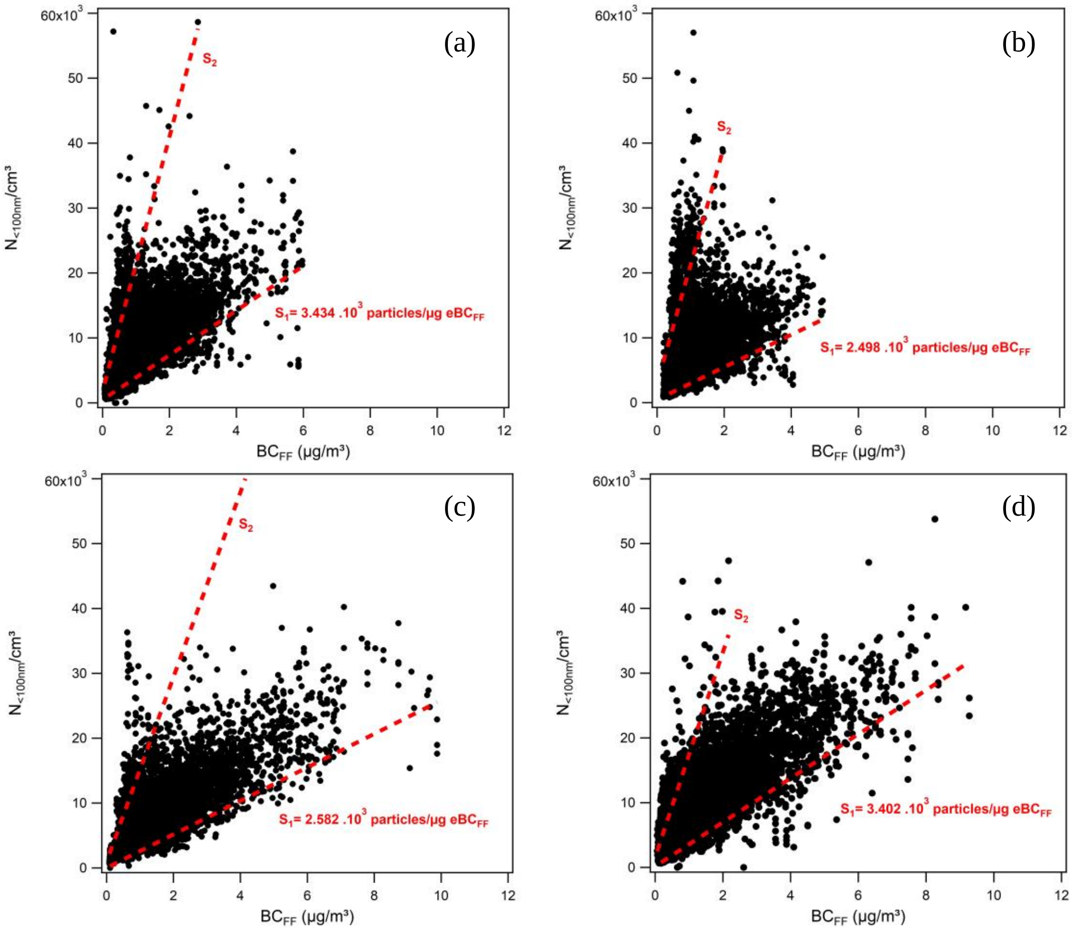


**Figure S7.** N (20 to 100 nm) from 3031 ultrafine particle monitor measurements vs $BC_{FF}$ scatter plot for spring (a), summer (b), autumn (c) and winter (d). BC data were smoothed with 1h-median to avoid spikes which can skew the linear regressions. S1 and S2 indicate the lines of the minimum and maximum slopes, respectively, which contain the N/BC ratio data.

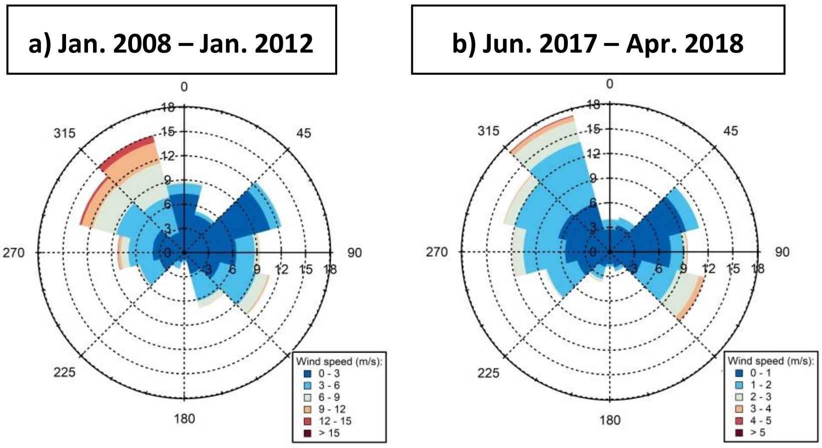


**Figure S8.** Wind roses for the hippodrome station (a) from January 2008 to January 2012 and MRS-LCP station (b) from June 2017 to April 2018. Tangential axe provide the wind direction (°) and radial axe the wind frequency (%). Wind direction clusters are color-coded according to the wind intensity (m.s$^{-1}$)

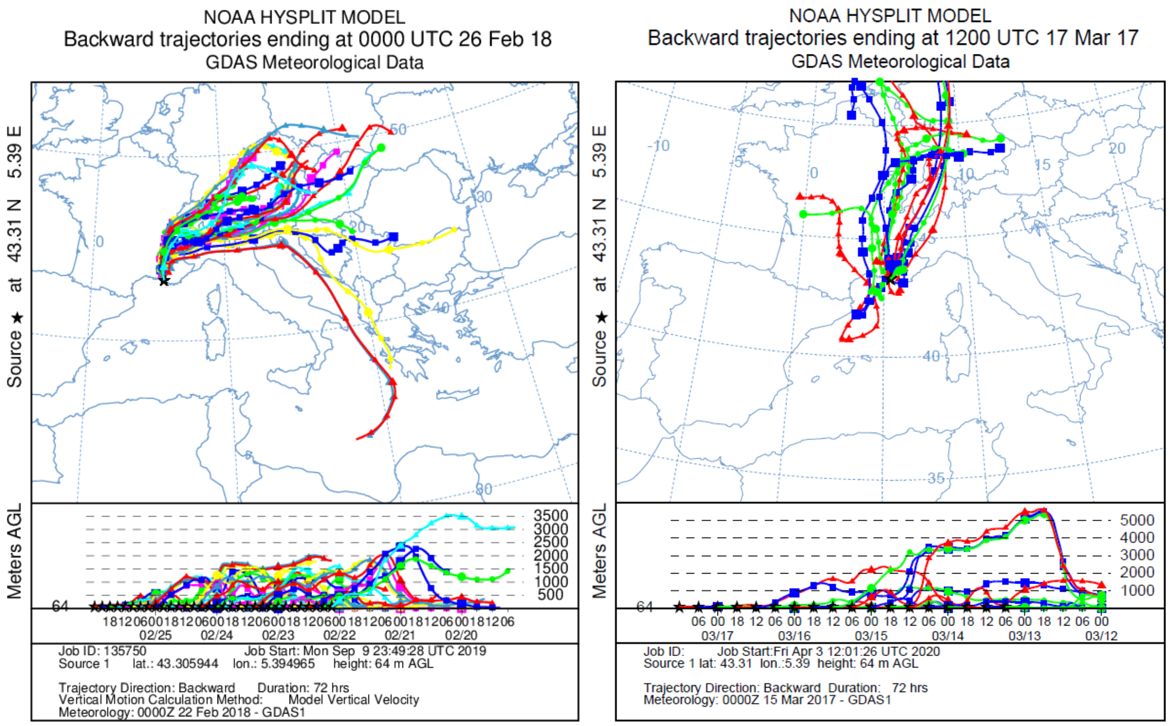


**Figure S9.** HYSPLIT air mass 72h-backtrajectories during the long-range episodes of February 2018 (left) and March 2017 (right) at MRS-LCP. The lower panels show the air mass altitudes (in meters AGL) over the time.

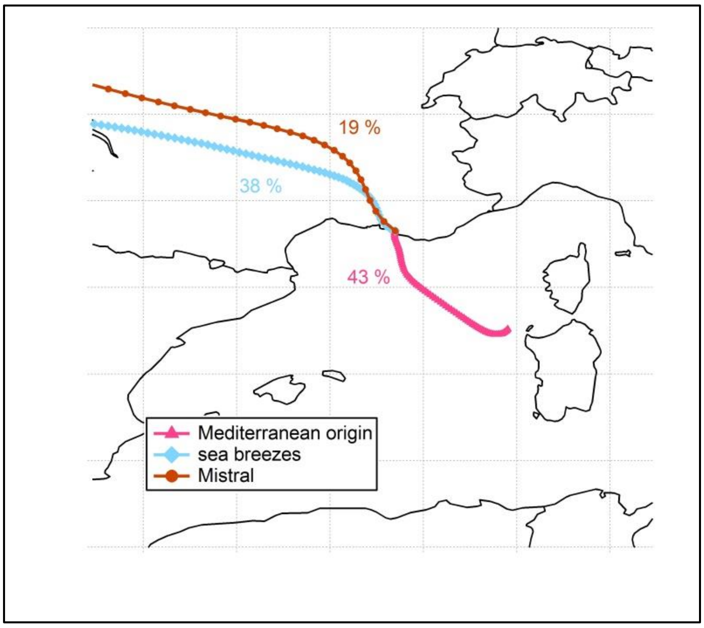


**Figure S10.** Mean Trajectories for the three summer clusters at MRS-LCP station. The colours of cluster represent different geographical origins and are used throughout this paper. Percentages indicate the proportion of trajectories compiled in each cluster.

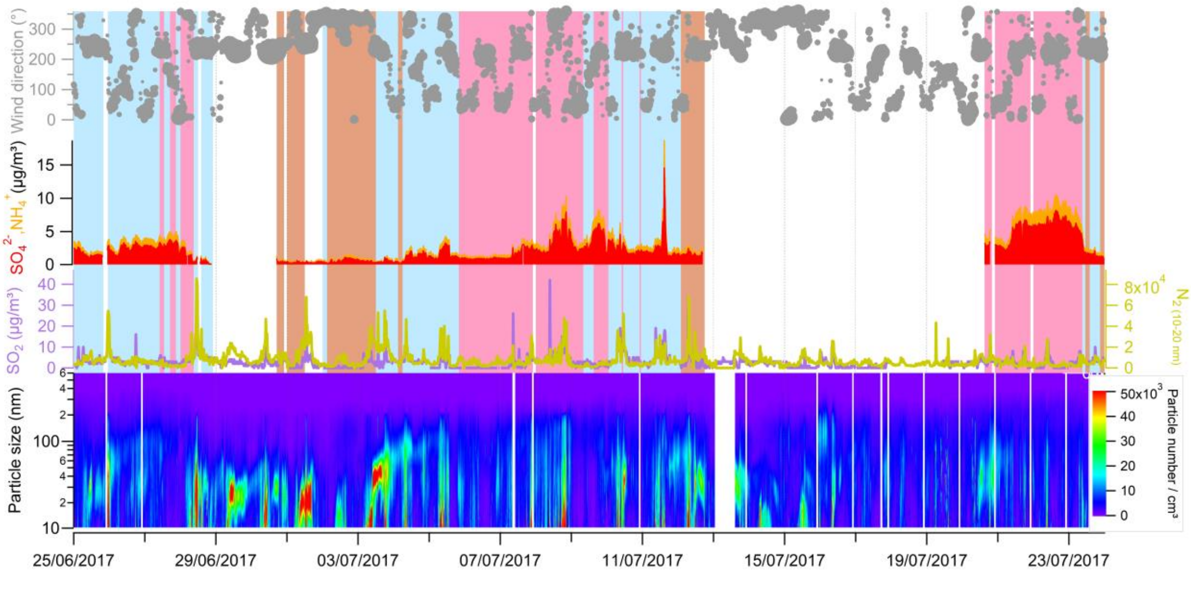


**Figure S11.** Time series of wind direction, $NH_4^+$, $SO_4^{2-}$, $SO_2$, $N_{2\,(10\text{-}20\ nm)}$ and particle total number measured with the SMPS GRIMM (10.25-600 nm) in summer (25 June to 23 July 2017). Background colours correspond to the classification of the three calculated clusters: Mediterranean origin (pink), sea breezes (light blue) and mistral wind (brown).

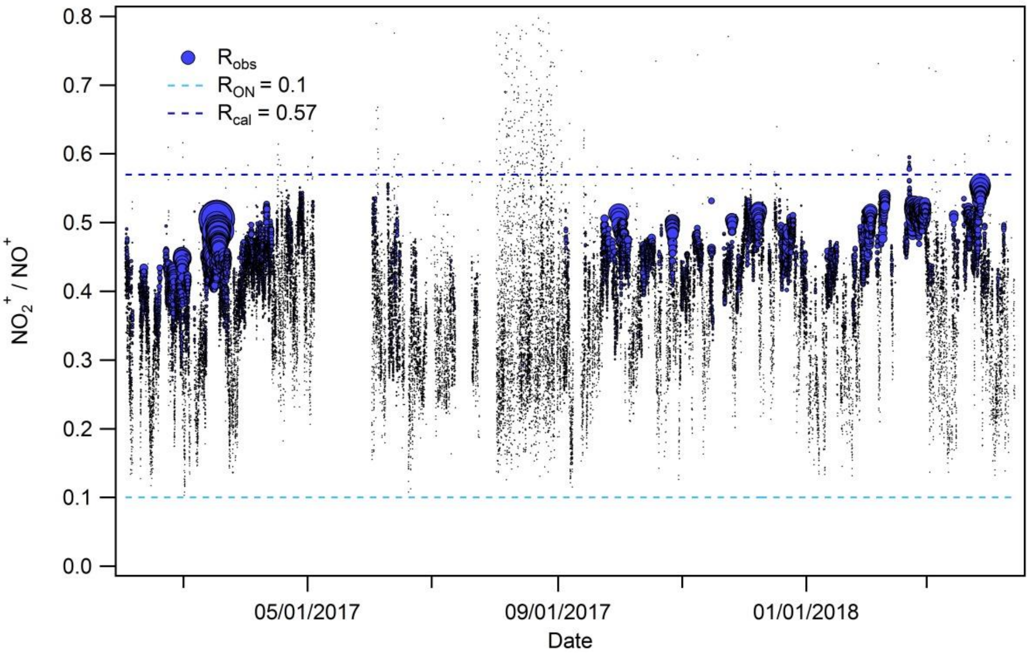


**Figure S12.** $NO_2^+/NO^+$ ratio over the measurement period. Marker sizes are proportional to the $NO_3^-$ concentrations. $R_{ON}$ dashed line is the ratio estimated for organic nitrates (minimum $NO_2^+/NO^+$ ratio observed on the dataset) and $R_{cal}$ dashed line represents the averaged ratio during ammonium nitrate calibrations.

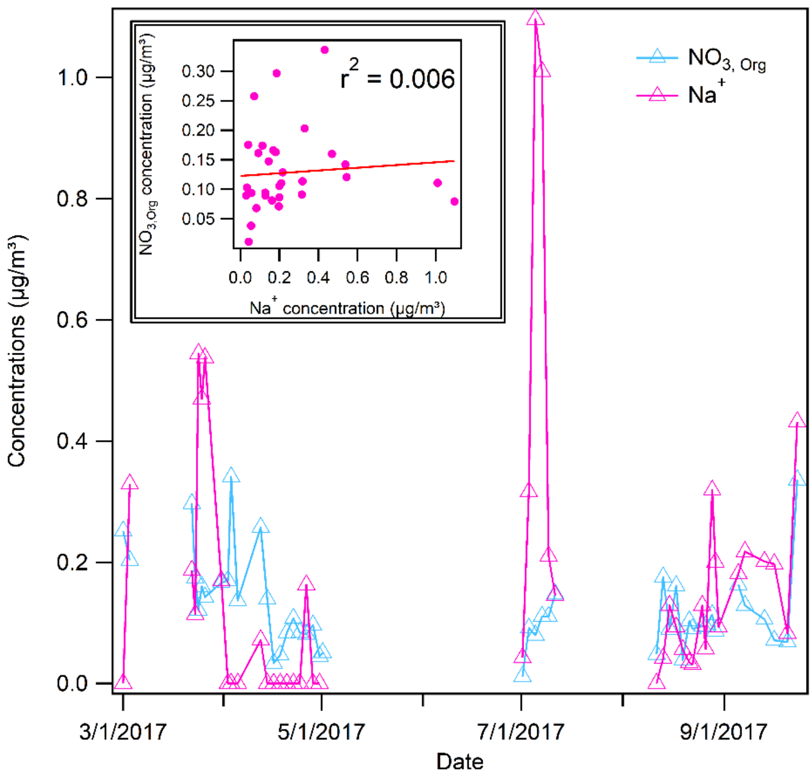


**Figure S13.** Comparison of $NO_{3,Org}$ calculated from ACSM data and $Na^+$ concentrations from $PM_1$ filters. Salts of nitrate such as $NaNO_3$ can be interfering inorganic species, with low $NO_2^+/NO^+$ ratio as for organic nitrates. Here there is no correlation between $Na^+$ and calculated $NO_{3,Org}$ variations over time.

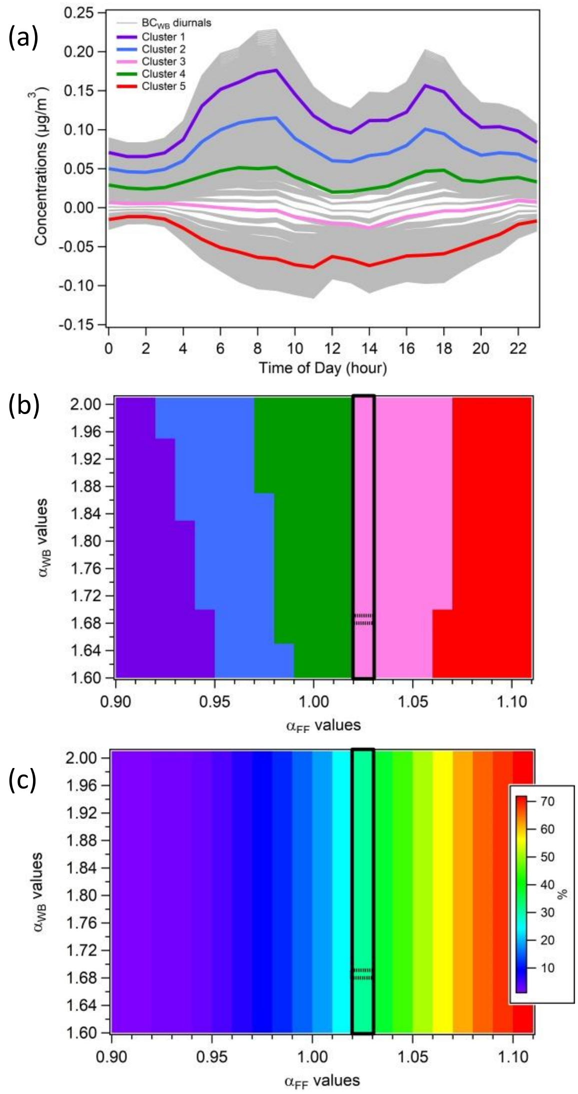


**Figure S14.** Cluster analysis of the BCWB diurnal cycles from "Kaddouz" station in summer 2017. Five clusters are presented according different colors (cluser 1 = violet; cluster 2 = blue; cluster 3 = pink; cluster 4 = green; cluster 5 = red). (a) represents all $BC_{WB}$ diurnals (in grey) from the sensitivity test and the colored cluster diurnals. (b) represents the cluster assignment for all Angström exponents combinations and (c) shows the number of $BC_{WB}<0$ points (in %) according to a rainbow color scale. For (b) and (c) the area surrounded with black line includes all accepted combinations, and the black dashed line correspond to the selected combination in this study ($\alpha_{FF}$=1.02 and $\alpha_{WB}$=1.68).

# SUPPLEMENTARY TEXT

## Description of the organic nitrate calculation from ToF-ACSM measurements

Many past studies have demonstrated the possibility to separate the contribution of inorganic ($NO_{3,Inorg}$) and organic nitrate ($NO_{3,Org}$) to the measured nitrate based on the ratio of $NO_2^+$ and $NO^+$ (Farmer et al., 2010; Fry et al., 2018; Kiendler-Scharr et al., 2016; Reyes-Villegas et al., 2018; Xu et al., 2015). Concentrations of $NO_{3,Org}$ were calculated following the method described by Farmer et al., 2010:

$$x_{NO_{3,Org}} = \frac{(R_{obs}-R_{cal})\,(1+R_{ON})}{(R_{ON}-R_{cal})\,(1+R_{obs})}, \qquad \text{(S1)}$$

where $R_{obs}$ is the ratio between m/z 46 and m/z 30 ($NO_2^+/NO^+$) observed over the dataset; $R_{cal}$ is the ratio during ammonium nitrate calibrations; and $R_{ON}$ is the ratio for organic nitrates. $R_{cal}$ = 0.56 is the average of all ammonium nitrate calibrations reported in table S3 (ratios between 0.56 and 0.57 during all the calibrations). Following Kiendler-Scharr et al. (2016) and Kostenidou et al. (2015), the minimum ratio $NO_2^+/NO^+$ observed for the dataset (0.1 , Figure S12) was selected for $R_{ON}$ . $R_{ON}$, $R_{cal}$ and $R_{ON}/R_{cal}$ values obtained were consistent with previously reported values (Boyd et al., 2015; Bruns et al., 2010; Farmer et al., 2010; Kiendler-Scharr et al., 2016). Finally, $NO_{3,Org}$ concentrations in µg.m$^{-3}$ were calculated as below:

$$NO_{3,Org} = x_{NO_{3,Org}}.NO_3^- , \qquad \text{(S2)}$$

where $NO_3^-$ is the total nitrate measured by the ToF-ACSM. We assume there is no interference from $CH_2O^+$ at m/z 30 and $CH_2O_2^+$ at m/z 46 as mentioned in section 2.2.1. This expression only applies if $NH_4NO_3$ is the major inorganic nitrate addition to organic nitrate in submicron particles. Some inorganics salts of nitrate such as $NaNO_3$ can give very small $NO_2^+/NO^+$ ratio especially for coastal site like Marseille, and could contribute to the observed $NO_2^+/NO^+$ ratio. Only concentrations of $Na^+$ were available with daily $PM_1$ filters measurements in 2017 and their different behaviour from $NO_{3,Org}$ daily concentrations let suppose that no interference comes from $Na^+$ (Figure S13).

The average $NO_{3,Org}$ fraction for the whole dataset was 20±7%. The error is determined from error propagation calculations described by Farmer et al. (2010) derived from the different ratios ($R_{obs}$, $R_{cal}$, $R_{ON}$) uncertainties. The standard error of the mean was used as uncertainty associated with $R_{obs}$ and $R_{cal}$ and an estimated uncertainty of ±20% was used for $R_{ON}$.

## K-means clustering analysis applied to the Angström exponent's selection

From this analysis a set of 861 combinations was evaluated and optimized based on the $BC_{WB}$ diurnal cycles, which must significantly differ from $BC_{FF}$ diurnal profiles. All the 861 diurnal cycles were categorized according to a k-means clustering analysis. This technique allowed to group the results into a specific number of clusters (Figure S14a) based on the protocols from Elser et al. (2016) and Bozzetti et al. (2017).

The analysis aims at classify a dataset into *k* clusters by minimizing the term T1 from the cost function (CF), which represents the sum of the Euclidian distances between each data point ($x_i$) and its respective cluster center $\mu_{zi}$ according to equation (S3). In order to select the right number of clusters the same strategy as Elser et al. (2016) and Bozzetti et al. (2017) is used. The goal is to explicitly penalize the addition of a new cluster by using the Bayesian information criteria, given as the product between the number of cluster *k* and the logarithm of the dimensionality of the clusters *D* (=24 here, which correspond to the number of hours from the diurnal cycles).

$$T1 = \sum_{i,z}\left((x_i - \mu_{z,i})^2\right) \ , \tag{S3}$$

$$CF = T1 + T2 = \sum_{i,z}\left((x_i - \mu_{z,i})^2\right) + k \, . \log{(D)} \ , \tag{S4}$$

At the end the cost function which has to be minimized is described in equation (S4). Figure S6a displays a minimum in the cost function at five clusters. Thus the 5 clusters solution was retained to describe the $BC_{WB}$ diurnal variability according to the different set of Angsröm exponents.

The diurnal evolutions of $BC_{WB}$ for different Angström exponent's $\alpha_{FF}$ and $\alpha_{WB}$ show a two-peak diurnal pattern typical of traffic similarly to $BC_{FF}$ when considering the clusters 1, 2 and 4. For cluster 5 diurnal cycle was negative suggesting wrong assignments of the model, while cluster 3 showed a smooth wood burning profile and reduced concentrations close to 0, which is expected for a kerbside site. The possible combinations of Angström exponents for this cluster are represented in Figure S14b (pink area).

To reduce the current multitude of possibilities a second criterion of selection is optimized, which is the minimum number of $BC_{WB}$<0 points (i.e. $BC_{FF}$>BC) as determined by Petit et al. (2017). Among the previous selection (cluster 3) this minimum number is inspected and found for an $\alpha_{FF}$ = 1.02 and an $\alpha_{WB}$ = {1.6; 2}. An $\alpha_{FF}$ of 1.02 would be more representative of fresh traffic emission in Marseille. As no more criterion allow to reduce $\alpha_{WB}$ , a reference value of 1.68 from Zotter et al. (2017) has been used for this study. Final diurnal evolutions for "Kaddouz" site are presented in Figure S6b.

Boyd, C. M., Sanchez, J., Xu, L., Eugene, A. J., Nah, T., Tuet, W. Y., Guzman, M. I. and Ng, N. L.: Secondary organic aerosol formation from the β-pinene+NO<sub>3</sub> system: effect of humidity and peroxy radical fate, Atmospheric Chem. Phys., 15(13), 7497–7522, doi:10.5194/acp-15-7497-2015, 2015.

Bozzetti, C., El Haddad, I., Salameh, D., Daellenbach, K. R., Fermo, P., Gonzalez, R., Minguillón, M. C., Iinuma, Y., Poulain, L., Elser, M., Müller, E., Slowik, J. G., Jaffrezo, J.-L., Baltensperger, U., Marchand, N. and Prévôt, A. S. H.: Organic aerosol source apportionment by offline-AMS over a full year in Marseille, Atmospheric Chem. Phys., 17(13), 8247–8268, doi:10.5194/acp-17-8247-2017, 2017.

Bruns, E. A., Perraud, V., Zelenyuk, A., Ezell, M. J., Johnson, S. N., Yu, Y., Imre, D., Finlayson-Pitts, B. J. and Alexander, M. L.: Comparison of FTIR and Particle Mass Spectrometry for the Measurement of Particulate Organic Nitrates, Environ. Sci. Technol., 44(3), 1056–1061, doi:10.1021/es9029864, 2010.

Elser, M., Huang, R.-J., Wolf, R., Slowik, J. G., Wang, Q., Canonaco, F., Li, G., Bozzetti, C., Daellenbach, K. R., Huang, Y., Zhang, R., Li, Z., Cao, J., Baltensperger, U., El-Haddad, I. and Prévôt, A. S. H.: New insights into PM$_{2.5}$ chemical composition and sources in two major cities in China during extreme haze events using aerosol mass spectrometry, Atmospheric Chem. Phys., 16(5), 3207–3225, doi:10.5194/acp-16-3207-2016, 2016.

Farmer, D. K., Matsunaga, A., Docherty, K. S., Surratt, J. D., Seinfeld, J. H., Ziemann, P. J. and Jimenez, J. L.: Response of an aerosol mass spectrometer to organonitrates and organosulfates and implications for atmospheric chemistry, Proc. Natl. Acad. Sci., 107(15), 6670–6675, doi:10.1073/pnas.0912340107, 2010.

Fry, J. L., Brown, S. S., Middlebrook, A. M., Edwards, P. M., Campuzano-Jost, P., Day, D. A., Jimenez, J. L., Allen, H. M., Ryerson, T. B., Pollack, I., Graus, M., Warneke, C., de Gouw, J. A., Brock, C. A., Gilman, J., Lerner, B. M., Dubé, W. P., Liao, J. and Welti, A.: Secondary organic aerosol (SOA) yields from NO<sub>3</sub> radical + isoprene based on nighttime aircraft power plant plume transects, Atmospheric Chem. Phys., 18(16), 11663–11682, doi:10.5194/acp-18-11663-2018, 2018.

Kiendler-Scharr, A., Mensah, A. A., Friese, E., Topping, D., Nemitz, E., Prevot, A. S. H., Äijälä, M., Allan, J., Canonaco, F., Canagaratna, M., Carbone, S., Crippa, M., Dall Osto, M., Day, D. A., De Carlo, P., Di Marco, C. F., Elbern, H., Eriksson, A., Freney, E., Hao, L., Herrmann, H., Hildebrandt, L., Hillamo, R., Jimenez, J. L., Laaksonen, A., McFiggans, G., Mohr, C., O'Dowd, C., Otjes, R., Ovadnevaite, J., Pandis, S. N., Poulain, L., Schlag, P., Sellegri, K., Swietlicki, E., Tiitta, P., Vermeulen, A., Wahner, A., Worsnop, D. and Wu, H.-C.: Ubiquity of organic nitrates from nighttime chemistry in the European submicron aerosol: Organic Nitrates in European PM1, Geophys. Res. Lett., 43(14), 7735–7744, doi:10.1002/2016GL069239, 2016.

Kostenidou, E., Florou, K., Kaltsonoudis, C., Tsiflikiotou, M., Vratolis, S., Eleftheriadis, K. and Pandis, S. N.: Sources and chemical characterization of organic aerosol during the summer in the eastern Mediterranean, Atmospheric Chem. Phys., 15(19), 11355–11371, doi:10.5194/acp-15-11355-2015, 2015.

Petit, J.-E., Amodeo, T., Meleux, F., Bessagnet, B., Menut, L., Grenier, D., Pellan, Y., Ockler, A., Rocq, B., Gros, V., Sciare, J. and Favez, O.: Characterising an intense PM pollution episode in March 2015 in France from multisite approach and near real time data: Climatology, variabilities, geographical origins and model evaluation, Atmos. Environ., 155, 68–84, doi:10.1016/j.atmosenv.2017.02.012, 2017.

Reyes-Villegas, E., Priestley, M., Ting, Y.-C., Haslett, S., Bannan, T., Le Breton, M., Williams, P. I., Bacak, A., Flynn, M. J., Coe, H., Percival, C. and Allan, J. D.: Simultaneous aerosol mass spectrometry and chemical ionisation mass spectrometry measurements during a biomass burning event in the UK: insights into nitrate chemistry, Atmospheric Chem. Phys., 18(6), 4093–4111, doi:10.5194/acp-18-4093-2018, 2018.

Xu, L., Suresh, S., Guo, H., Weber, R. J. and Ng, N. L.: Aerosol characterization over the southeastern United States using high-resolution aerosol mass spectrometry: spatial and seasonal variation of aerosol composition and sources with a focus on organic nitrates, Atmospheric Chem. Phys., 15(13), 7307–7336, doi:10.5194/acp-15-7307-2015, 2015.

Zotter, P., Herich, H., Gysel, M., El-Haddad, I., Zhang, Y., Močnik, G., Hüglin, C., Baltensperger, U., Szidat, S. and Prévôt, A. S. H.: Evaluation of the absorption Ångström exponents for traffic and wood burning in the Aethalometer-based source apportionment using radiocarbon measurements of ambient aerosol, Atmospheric Chem. Phys., 17(6), 4229–4249, doi:10.5194/acp-17-4229-2017, 2017.